Clim Dyn (2017) 48:3583–3597
DOI 10.1007/s00382-016-3285-2

Effective control parameters in a deep convection scheme for improved simulation of the Madden–Julian oscillation

Jin-Ho Choi[1] · **Kyong-Hwan Seo**[1]

Received: 22 February 2016 / Accepted: 16 July 2016 / Published online: 26 July 2016

Abstract This work seeks to find the most effective parameters in a deep convection scheme (relaxed Arakawa–Schubert scheme) of the National Centers of Environmental Prediction Climate Forecast System model for improved simulation of the Madden–Julian Oscillation (MJO). A suite of sensitivity experiments are performed by changing physical components such as the relaxation parameter of mass flux for adjustment of the environment, the evaporation rate from large-scale precipitation, the moisture trigger threshold using relative humidity of the boundary layer, and the fraction of re-evaporation of convective (subgrid-scale) rainfall. Among them, the last two parameters are found to produce a significant improvement. Increasing the strength of these two parameters reduces light rainfall that inhibits complete formation of the tropical convective system or supplies more moisture that help increase a potential energy to large-scale environment in the lower troposphere (especially at 700 hPa), leading to moisture preconditioning favorable for further development and eastward propagation of the MJO. In a more humid environment, more organized MJO structure (i.e., space–time spectral signal, eastward propagation, and tilted vertical structure) is produced.

Keywords Madden–Julian oscillation · NCEP CFS model · RAS deep convection scheme · Critical relative humidity of the boundary layer · Fraction of re-evaporation of convective precipitation

✉ Kyong-Hwan Seo
khseo@pusan.ac.kr

[1] Division of Earth Environmental System, Department of Atmospheric Sciences, Pusan National University, Busan 609-735, South Korea

1 Introduction

The Madden–Julian Oscillation (MJO) is the most prominent mode of tropical intraseasonal (30–90 days) variability (Madden and Julian 1994; Zhang 2013) and affects the weather and climate over the globe, including the initiation and withdrawal of the Indian and Australian monsoon systems (Wheeler and McBride 2005), modulation of tropical cyclones (Maloney and Hartmann 2000; Kim and Seo 2016), formation of extratropical circulation anomalies through teleconnections (Seo and Son 2012), and some El Niño events (Takayabu et al. 1999).

Despite its significant impact on global climate and weather, most contemporary general circulation models (GCMs) suffer from difficulties in realistically simulating the MJO (Lin et al. 2006; Seo et al. 2007; Seo and Wang 2010; Hung et al. 2013; Kim et al. 2014; Jiang et al. 2015). Hung et al. (2013) demonstrated that seven out of 20 coupled GCMs, participating in the Intergovernmental Panel on Climate Change (IPCC) Fifth Assessment Report (AR5), are able to produce a MJO-like variance and a pronounced 30–70-day period spectral peak. However, only one model reproduced a realistic eastward propagation of the MJO. Furthermore, Jiang et al. (2015) showed that only eight out of 27 models used in the MJO Task Force (MJOTF) and GEWEX Atmospheric System Study (GASS) Global MJO Model Comparison Project, are able to capture dominant signals of MJO propagation.

Deficiencies and uncertainties in MJO simulation stem from a deep convection parameterizations, which are one of the most important issues in the climate modeling community. For example, Wang and Schlesinger (1999) showed that increasing the relative humidity threshold in a deep convection scheme leads to the improved MJO simulation. The MJO evaluation in the IPCC AR5 models

by Hung et al. (2013) demonstrated that GCMs using convective triggers linked to low-level moisture convergence can simulate the MJO well. Recently, it has been widely documented that the MJO is considered a moisture mode (Sobel et al. 2001; Sobel and Maloney 2012, 2013) and a robust relationship between deep convection and environmental moisture has been found in observations (Bretherton et al. 2004) and modeling studies (Thayer-Calder and Randall 2009; Kim et al. 2014; Hagos et al. 2014, 2016). Kim et al. (2014) suggested that MJO simulation skill is significantly correlated with moisture–convection sensitivity. Therefore, it is important to investigate the physical relationship between convection and moisture for robust MJO simulations.

In this study, we investigate control parameters (such as thresholds related to moisture triggers and the fraction of re-evaporation of convective rainfall) in a deep convection scheme for an improved simulation of the MJO, using the National Centers for Environmental Prediction (NCEP) Climate Forecast System (CFS) model with a relaxed Arakawa–Schubert (RAS) (Arakawa and Schubert 1974; Moorthi and Suarez 1999) cumulus scheme. A previous study by Seo and Wang (2010) showed that this version of the model produces a much-improved tropical intraseasonal oscillation, but that the model deficiencies still exist. We have conducted a variety of sensitivity experiments with the RAS scheme by modifying physical components such as the relaxation parameter of mass flux for adjustment of the environment, the evaporation rate from large-scale precipitation, the moisture trigger threshold using relative humidity of the boundary layer, and the fraction of re-evaporation of convective (subgrid-scale) rainfall. Among them, only the last two parameters are selected for the evaluation because no sensitivity appears in the other parameters.

Section 2 portrays the models, experimental configuration, and observational data. The distribution of the reasonable mean state precipitation, and relationship between environmental moisture and convection for the realistic MJO simulation are presented in Sect. 3. In Sect. 4, results from the sensitivity simulations that seek to understand the characteristics of the horizontal and vertical organization are described. Finally, the summary and discussion are given in Sect. 5.

2 The CFS model, experiment and observations

The NCEP's coupled ocean–atmosphere CFS model (Saha et al. 2006) is used in this study. The atmospheric component (the Global Forecast System model) adopts a spectral truncation of 62 waves (T62) in the horizontal (~209 km) and a finite differencing in the vertical with 64 sigma layers. The oceanic component is the Geophysical Fluid Dynamics Laboratory Modular Ocean Model version 3 (Pacanowski and Griffies 1998).

The RAS scheme invoked in this study is an updated version of the original scheme (Moorthi and Suarez 1992), which includes convective downdrafts (Cheng and Arakawa 1997a, b), evaporation of falling precipitation (Sud and Molod 1988), and an improved cloud updraft model. In particular, the RAS scheme considers multiple cloud types with relaxed quasi-equilibrium states, and allows updraft detrainment at different cloud tops. In addition, a threshold of relative humidity of the boundary layer is added as a trigger function of convection initiation.

A series of sensitivity experiments were conducted by applying different values of critical relative humidity (RH) of the boundary layer for convection triggering. Threshold values of 65.0 % (RH65), 75.0 % (RH75, control run), 80.0 % (RH80), 82.5 % (RH825), and 85.0 % (RH85) are used. We regard higher values of the critical RH as more stringent triggers, which make it harder for deep convection to be initiated. Two additional simulations are performed to investigate the sensitivity to a fraction of re-evaporation of convective precipitation: the weakened case (Reevap_W) was set to be about one-tenth of its original fraction, while the strengthened case (Reevap_S) was configured to be twice the original fraction (see Table 1). Note that as the fraction of re-evaporation of falling rainfall increases, more enhanced deep convection occurs in a more humid atmosphere. The exact formalism related to this process can be found in Moorthi and Suarez (1999) (see their Eqs. 102–103). A summary of the experimental design is shown in Table 1. Note that uncoupled (atmosphere-alone) model experiments were performed by applying the same variations as those for coupled runs, but all simulations showed stationary or westward-moving intraseasonal disturbances. Also, these simulations produced more overreddened variance (no isolating intraseasonal power) and weaker dynamic–thermodynamic organization than the coupled ones. For these reasons, we adopt the coupled atmosphere–ocean CFS model in this study.

Simulations were initiated from the observed analysis of 1 January 1984 and run for six years. Only the last 5 years of model output were analyzed. Note that all CFS simulations in this study exhibit one El Niño event and one La Niña event over the NINO 3.4 region (5°S–5°N, 170°W–120°W) during the integration time period, implying that the simulated sea surface temperature (SST) anomaly over this region does not drift towards perpetual El Niño or La Niña state. The observational data used in this study consist of the daily outgoing longwave radiation (OLR) data from the National Oceanic and Atmospheric Administration (NOAA) polar-orbiting series of satellites (Liebmann and Smith 1996), the Global Precipitation Climatology Project, version 1.1 (GPCP v1.1) (Huffman

Table 1 Experimental details for the NCEP CFS model simulations

Experiment Name[a]	Critical relative humidity[b] (%)	Fraction of re-evaporation of falling convective precipitation
RH65	**65.0**	Normal
RH75 (CTRL)	**75.0**	Normal
RH80	**80.0**	Normal
RH825	**82.5**	Normal
RH85	**85.0**	Normal
Reevap_W	75.0	**Weak**[c]
Reevap_S	75.0	**Strong**[d]

Bold indicates the modified parameters in each simulation

[a] The Relaxed Arakawa–Schubert (RAS) cumulus scheme is applied to all experiments

[b] Convection occurs when relative humidity of the boundary layer equals or exceeds a critical value

[c] Fraction of re-evaporation of falling convective rainfall is reduced to one-tenth of the original value

[d] Fraction of re-evaporation of falling convective rainfall is doubled

et al. 2001), and the European Centre for Medium-Range Weather Forecasts (ECMWF) Interim Re-Analysis (ERAI) (Dee et al. 2011). The data period is from 1997 to 2006.

All datasets are regridded into a 2.5° by 2.5° longitude–latitude grid to match the CFS output. Daily anomalies for all datasets are calculated by subtracting the time mean and the first three harmonics.

3 Relationship between environmental moisture and convection

According to previous studies of the MJO (Kim et al. 2009; Jiang et al. 2015), a reasonable mean state precipitation is necessary for the realistic MJO simulation. Figure 1 shows annual-mean precipitation from observation (GPCP) and NCEP CFS simulations. Most of the CFS runs struggle with a double inter-tropical convergence zone (ITCZ) over the western Pacific and excessive rainfall over the Indian Ocean and the Maritime Continent. However, as the moisture trigger or the fraction of re-evaporation of precipitation is strengthened, although the climatological-mean precipitation pattern for most of RH experiments (Fig. 1c–e) does not change much from the control simulation (Fig. 1b), the mean pattern in Reevap_S (Fig. 1h) is improved with a significant reduction in wet bias over the Indian Ocean and the western Pacific.

Contemporary climate models used in the Phase 3 and Phase 5 of the Coupled Model Intercomparison Project (i.e., CMIP3 and CMIP5) have produced frequent light rainfall (0.1–10 mm day^{-1}) that inhibits complete formation of the tropical convective cloudiness (Xavier 2012; Kim et al. 2014). Accordingly, the frequency of background precipitation rate needs to be examined. The distribution of precipitation over the equatorial warm pool region (10°S–10°N, 50°–180°E) as a function of accumulated percentiles (divided by the lower 80th and upper 20th percentiles) is presented in Fig. 2, which shows that zero precipitation in GPCP accounts for about 36 % (Fig. 2a). As the more stringent RH threshold is applied as a trigger function, large percentiles for no rainfall appear; 21 % for RH65, 22 % for RH75 (CTRL), 31 % for RH80, 42 % for RH825, and 44 % for RH85. Since 80 % of total precipitation in the sensitivity experiments corresponds to ~10 mm day^{-1} (upper limit of light (0.1–10 mm day^{-1}) rainfall), the frequency of light rainfall can be estimated by subtracting the percentage of no rainfall. This results in light rainfall representing only ~35–40 % of the total precipitation for RH85 and RH825, whereas the RH65, RH75 (CTRL), and RH80 simulations produce light rainfall making up ~50–60 % of the total precipitation. Note that sensitivity experiments associated with the relaxation parameter of mass flux for adjustment of the environment and the evaporation rate from large-scale precipitation also show higher rate of light rainfall similar to RH75 (CTRL) (not shown). Overall, the RH825 simulation shows a frequency distribution that most closely matches the GPCP data (Fig. 2a) and the overly frequent light rainfall occurs for the experiment with the less stringent RH threshold. From the distribution of the higher rainfall intensities (Fig. 2b), it is evident that more intense precipitation (Fig. 2b) is generated as the moisture trigger or the fraction of re-evaporation of convective rainfall is strengthened.

To provide additional details regarding the relationship between moisture and convection, composite vertical profiles of the RH as a function of daily average rainfall over the tropical warm pool region are presented in Fig. 3. In the observation (Fig. 3a), as the rainfall intensity increases, the lower troposphere becomes more humid, and the entire column is fully saturated for precipitation amounts greater than 25 mm day^{-1}. That

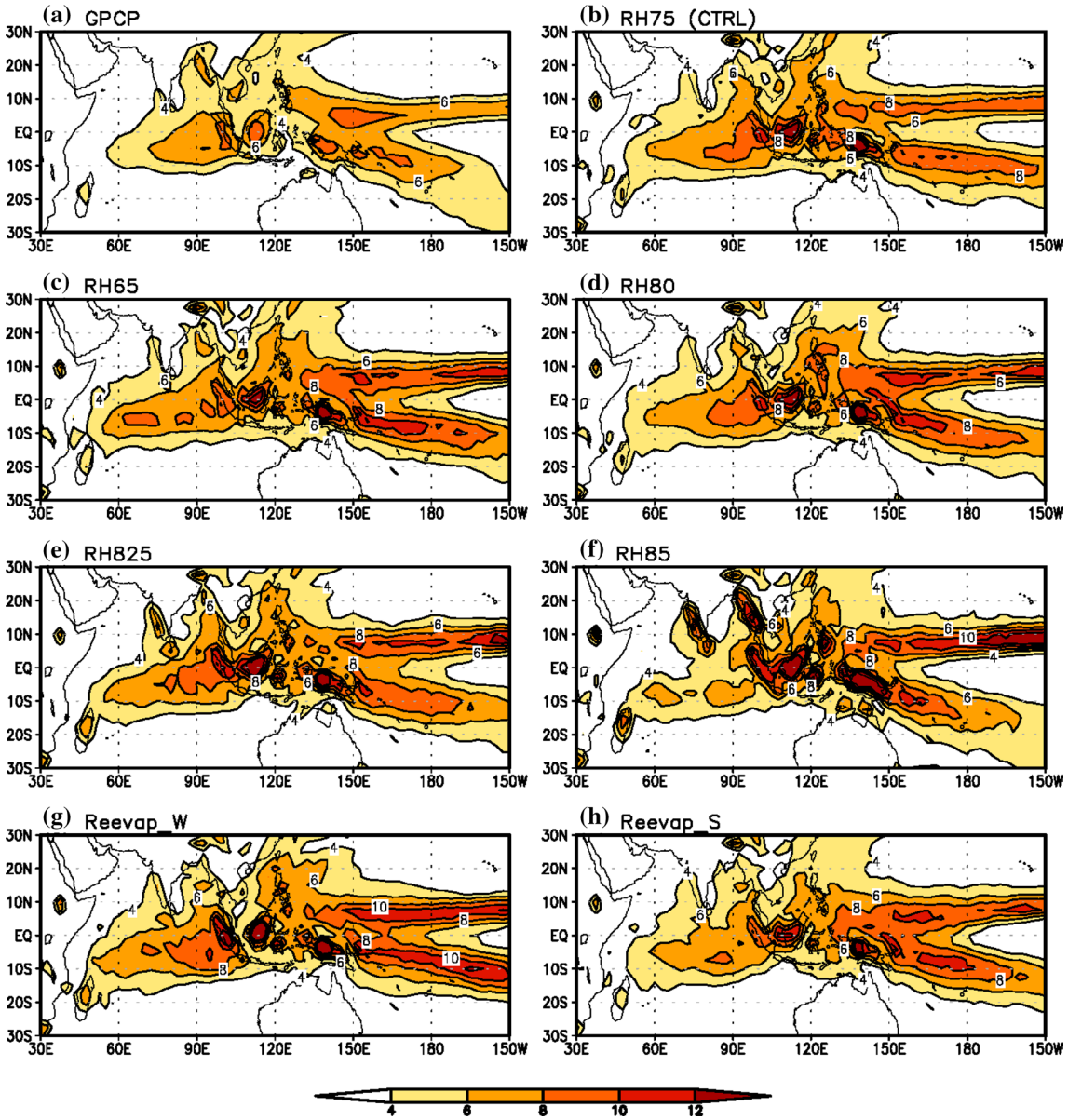

Fig. 1 Annual-mean precipitation (contours; intervals of 2 mm day^{-1} starting at 4 mm day^{-1}) from **a** GPCP and **b**–**h** NCEP CFS simulations: **b** RH75 (control run; CTRL), **c** RH65, **d** RH80, **e** RH825, **f** RH85, **g** Reevap_W, and **h** Reevap_S

is, heavier rainfall is suppressed until the atmosphere becomes nearly saturated with relative humidity higher than 70 % (shown as dotted contours). This is similar to the previous finding of Bretherton et al. (2004), who showed that more convective rainfall develops in a more humid atmosphere (i.e., moisture–convection feedback). Compared to the observation (Fig. 3a), RH75 (CTRL) (Fig. 3b) shows a much drier atmosphere for low precipitation intensity (~1 mm day^{-1}); this dry bias can be seen in many contemporary climate models. Also, a wet bias is observed in the lower to middle troposphere for moderate to heavier rainfall (>10 mm day^{-1}). This means that the updated RAS scheme that includes realistic physical processes (e.g., convective downdrafts, evaporation of falling rainfall, and improved convective structure), leads to the improved vertical moistening structure than the original version (Moorthi and Suarez 1999). However, as the moisture trigger or the fraction of re-evaporation of precipitation becomes stronger, certain precipitation rate occurs in a more humid environment (Fig. 3b–h). In particular, experiments with a more stringent moisture trigger (RH825 and RH85) exhibit more humid regions in the lower troposphere (between 900 and 700 hPa) for light rainfall (0.1–10 mm day^{-1}) (Fig. 3e, f), and the

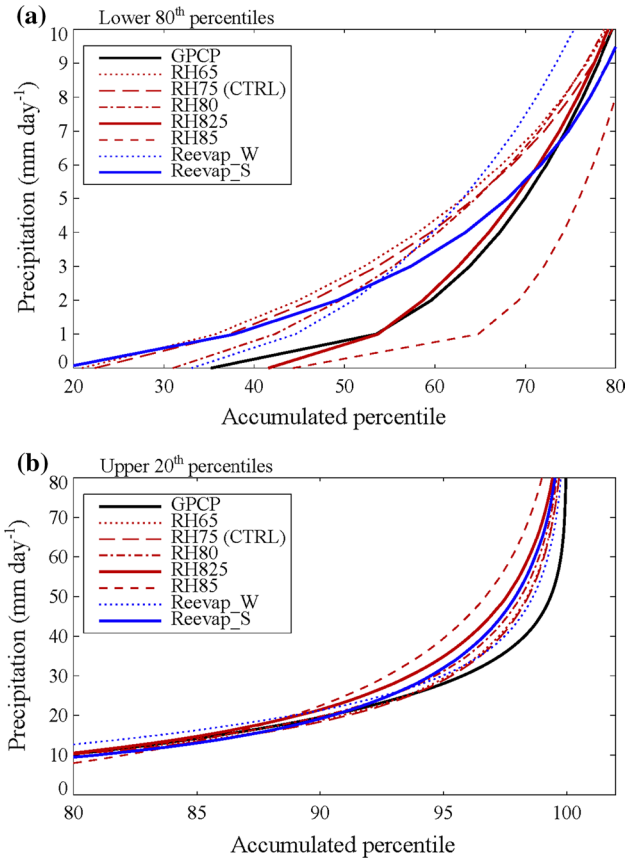

Fig. 2 Histogram of precipitation (mm day^{-1}) over the equatorial warm-pool region (10°S–10°N, 50°–180°E) as a function of accumulated percentiles. **a** Lower 80th percentiles, and **b** upper 20th percentiles are plotted

experiment with a stronger re-evaporation of convective rainfall (Fig. 3h) shows more moist areas in the boundary layer to the middle troposphere (surface to 500 hPa) for moderate to heavier rainfall (>10 mm day^{-1}) (Fig. 3h).

To further clarify this difference of moist environment, Fig. 4 shows the composite vertical profiles of difference in relative humidity between sensitivity simulations and the RH75 (CTRL). In contrast to RH75 (CTRL), RH825 (Fig. 4a) and RH85 (Fig. 4b) produce a maximum humid environment in the lower troposphere for light rainfall regime. Although humid regions exist in the upper troposphere (about 300 hPa), these two simulations still show dry biases compared with the observation (Fig. 3d, f). This moistening in the lower troposphere represents a reduction in the frequency of light precipitation due to a more stringent moisture trigger (see Fig. 2a). For the simulation with re-evaporation of convective rainfall, Reevap_W (Fig. 4c) shows an overall dry bias for moderate to heavier rainfall, whereas Reevap_S (Fig. 4d) reproduces moist column for generally all rain rates. In particular, the moist regime is concentrated at the lower troposphere (about 700 hPa). Also, the RH in moderate to heavier regime increases relative to a light rainfall regime (see Fig. 3h). This is related to more organized intense rainfall through more humid environment. This result suggests that a rigorous moisture trigger and stronger fraction of re-evaporation of convective precipitation may be critical factors for the realistic moisture–convection feedback.

An additional simulation is conducted to assess the combined effects of the two experiments (i.e., RH825 and Reevap_S) that produce a favorable humid environment for deep convection (not shown). Interestingly, this simulation produces an overly moist column for all rainfall intensities (especially at 700 hPa). However, this simulation shows an overreddened signal (>100 days), weaker moisture preconditioning, and lack of top-heavy heating (cooling in the entire column) in the deep convection phase. Due to complex interactions between physical processes in the deep convection scheme, the cause for this degeneration remains unanswered and this will be investigated in detail in the near future.

4 Sensitivity of simulated MJO

To check the dominant MJO-related spectral signals, we examine the signal-to-noise ratio of the observed and modeled convection (OLR) anomalies using the methodology of Wheeler and Kiladis (1999). Figure 5 shows the signal-to-noise ratio in the wavenumber–frequency spectral domain of symmetric components of the observed and simulated OLR anomalies. Only spectra of symmetric components are presented, as the characteristics of the antisymmetric spectra are similar. In the observation (Fig. 5a), westward-moving equatorial Rossby (ER) waves emerge, and eastward-moving MJO and Kelvin waves with stronger amplitude are verified. The observed MJO signal is evident in the intraseasonal band of 30–80-day periods (and wavenumbers 1–3) with a center at around 40–50 days and zonal wavenumber 1. The RH65 (Fig. 5c), RH75 (Fig. 5b), RH80 (Fig. 5d), and Reevap_W (Fig. 5g) display the MJO spectral peak existing at periods of 70–90 days and wavenumbers 2–4, and hence, they tend to have higher signal-to-noise ratio at slightly lower frequencies (which originates from part of red background noise as suggested by Lin et al. (2006)) and higher wavenumbers than the observation. Note that when the relaxation parameter of mass flux for adjustment of the environment and the evaporation rate from large-scale precipitation are modified, spectral signals in these simulations are similar to the RH75 (not shown). However, the spectral signal-to-noise ratio for RH825 (Fig. 5e) shows that the dominant variance is concentrated in an eastward-propagating signal at periods near 50 days and wavenumber 1, but with weaker magnitude. Compared with the RH825 simulation,

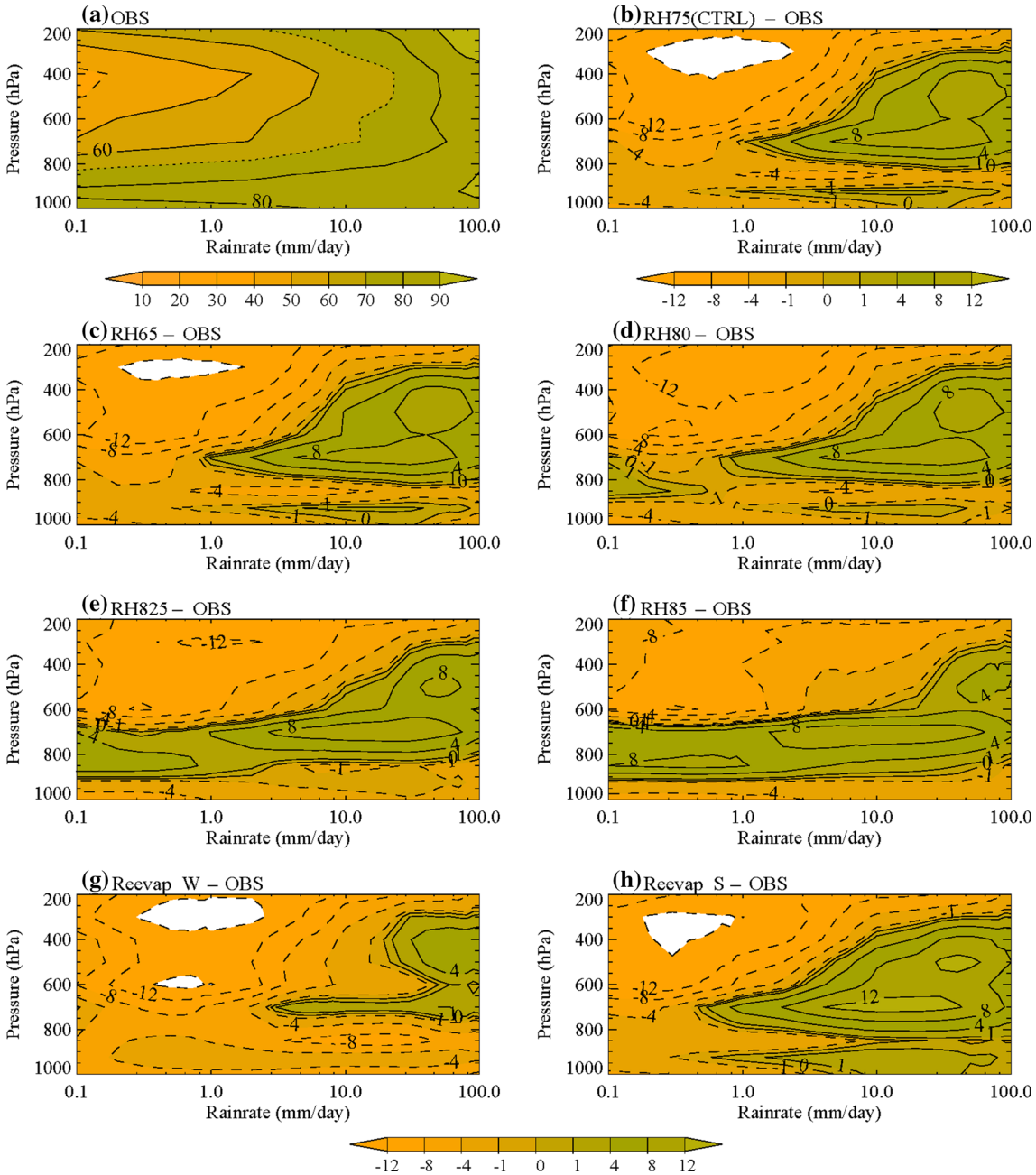

Fig. 3 Composite vertical profiles of relative humidity categorized by daily average rainfall over the tropical warm-pool region (10°S–10°N, 50°–180°E) for **a** observations (OBS) (contour intervals of 10 %) and **b**–**h** vertical profiles of the difference in relative humidity (contour intervals shown in the lower color bar) between observations and simulations; **b** RH75 (CTRL), **c** RH65, **d** RH80, **e** RH825, **f** RH85, **g** Reevap_W, and **h** Reevap_S. In (**a**), the 70 % contour line is *dotted* for clarity

RH85 (Fig. 5f) has higher frequencies (~30 days). The other two experiments, Reevap_W (Fig. 5g), and Reevap_S (Fig. 5h), show that as the fraction of re-evaporation of convective rainfall is strengthened, the MJO signal becomes stronger with realistic frequencies (55 days for Reevap_S), similar to the observation.

We further investigate the horizontal and vertical MJO structures by regressing onto a time series of the 20–90 day bandpass-filtered OLR averaged over the equatorial Indian Ocean (5°S–5°N, 75°–85°E). Note that results are similar for time series based on the western Pacific (5°S–5°N, 130°–150°E) (not shown). The regressed OLR in the longitude–time domain is illustrated in Fig. 6. The negative OLR anomaly (i.e., enhanced convection) moves eastward from the Indian Ocean to the dateline at a speed of about 4 m s^{-1} in RH825 (Fig. 6e) and Reevap_S (Fig. 6h), comparable to

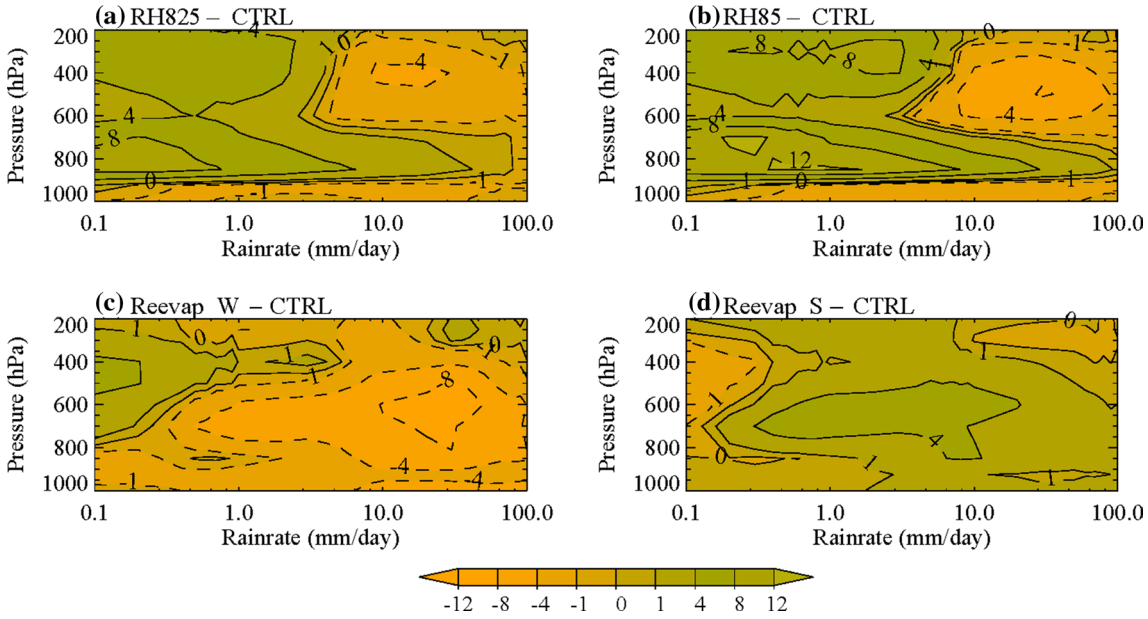

Fig. 4 As in Fig. 3, but for vertical profiles of the difference in relative humidity between RH75 (CTRL) and other simulations: **a** RH825, **b** RH85, **c** Reevap_W, and **d** Reevap_S

the observation (Fig. 6a). However, the other models tend to exhibit too slow eastward-propagating signals (i.e., phase speed of about 2.5 m s^{-1}), which are represented in the intraseasonal variance shifted toward the lower frequencies (>80 days) in Fig. 5. In addition, westward-moving signals are found over the western Pacific (especially, Fig. 6c, d, and f).

Vertical profiles of regressed specific humidity at lag day 0 are shown in Fig. 7. In the observation (Fig. 7a), shallow moistening to the east of enhanced convection grows up to 700 hPa, making a favorable condition for subsequent deep convection. During and after deep convection, deep moistening develops in the entire troposphere (700–300 hPa) with a peak near 650 hPa, while drying appears in the lower troposphere (below 600 hPa). In particular, the models (both RH825 and Reevap_S) that perform better in the moisture–convection feedback and the MJO spectral structure (Fig. 7e and h) exhibit abundant low-level moistening prior to intense deep convection and a gradual upward development of moisture anomalies, in agreement with the observation. Note that there is no sensitivity to differences in the integration level (e.g., 1000–850 or 1000–100 hPa) because a large amount of moisture resides in the lower troposphere (below 600 hPa). As described above, low-level moistening ahead of enhanced convection is also well simulated in the RH825 and Reevap_S (Fig. 8a). West of deep convection, drying signature in these two simulations is well captured although the magnitude is larger than the other simulations and observation. Furthermore, the positive MSE anomalies in the lower troposphere to the east of deep convection (Fig. 8b), which act to supply richer energy to the well-organized convection, are similar to the observation. This is consistent with the recharge–discharge theory by Bladé and Hartmann (1993) and Kemball-Cook and Weare (2001).

To explain the reason for a better MJO simulation in the RH825 and Reevap_S, vertical profiles of regressed apparent convective heating, Q_1 (Yanai et al. 1973), are presented in Fig. 9. Note that Q_1 is averaged over preconditioning (120°–135°E) and trailing (50°–65°E) regions to represent the robust heating structure before and after the enhanced MJO convection. In Fig. 9b, a typical bottom-heavy heating structure over the preconditioning region is observed in the lower troposphere with a maximum amplitude near 850 hPa, while RH75 (CTRL) displays no shallow heating in the lower troposphere and almost cooling throughout the atmospheric column. However, RH825 and Reevap_S show a structure similar to the observation, even though peak heating is weaker than in the observation. Wu (2003) proposed that a shallow (bottom-heavy) heating profile associated with a preconditioning signal drives a stronger low-level moisture convergence. For this, column-integrated (surface to 850 hPa) moisture convergence $\left(-\nabla \cdot (q\vec{v})\right)$ is calculated (not shown) and both RH825 and Reevap_S show somewhat stronger low-level moisture convergence prior to intense convection than the other simulations. To the west of the enhanced convection (Fig. 9a), top-heavy heating related to the second baroclinic structure is evident, because condensational heating associated with stratiform clouds occurs mainly in the upper and middle troposphere (with a peak near 400 hPa) and cooling develops in the

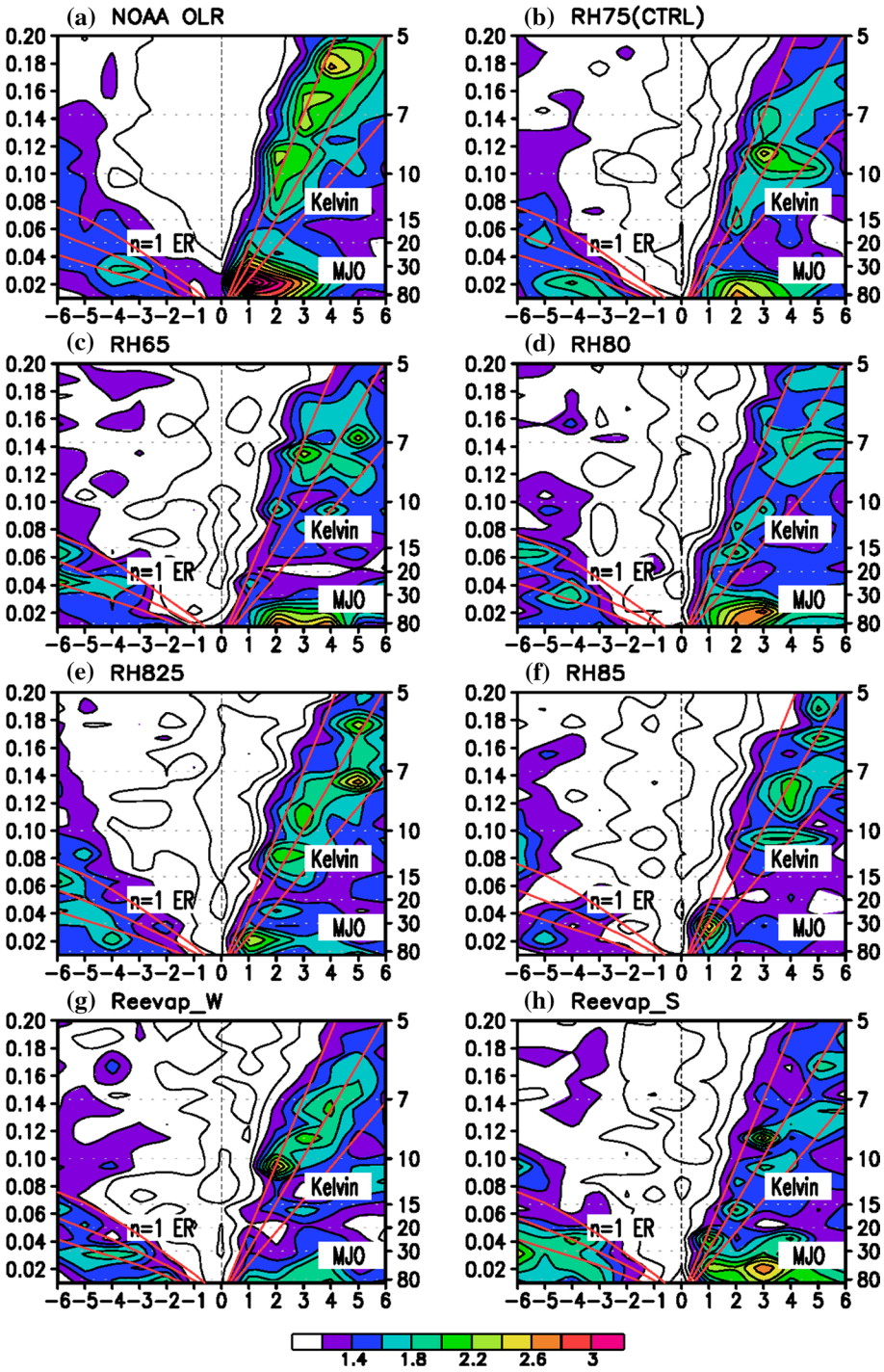

Fig. 5 Signal-to-noise ratio in the wavenumber–frequency spectral domain of the 15°S–15°N symmetric components of OLR anomalies for **a** NOAA OLR, **b** RH75 (CTRL), **c** RH65, **d** RH80, **e** RH825, **f** RH85, **g** Reevap_W, and **h** Reevap_S. Dispersion curves of the tropical waves are superimposed for the three equivalent depths of 12, 25, and 50 m (where the uppermost line is 50-m equivalent depth). The contour interval is 0.2 $W^2\ m^{-4}$, and shading begins at a value of 1.2 $W^2\ m^{-4}$

lower troposphere (below 650 hPa for only the observation and Reevap_S).

5 Summary and discussion

To investigate the effect of control parameters in a deep convection scheme for the proper simulation of the MJO, a series of experiments were performed with the NCEP CFS model employing the RAS convection scheme by modifying a moisture triggering parameter and a fraction of re-evaporation of convective precipitation. In the basic state, the former is related to a reduction of frequent light rainfall (0.1–10 mm day^{-1}) due to stringent convective triggers (requirement of more moisture in the lower troposphere between 900 and 700 hPa) and the latter produces a more humid environment from the boundary layer to middle troposphere (especially at 700 hPa) for moderate to heavier

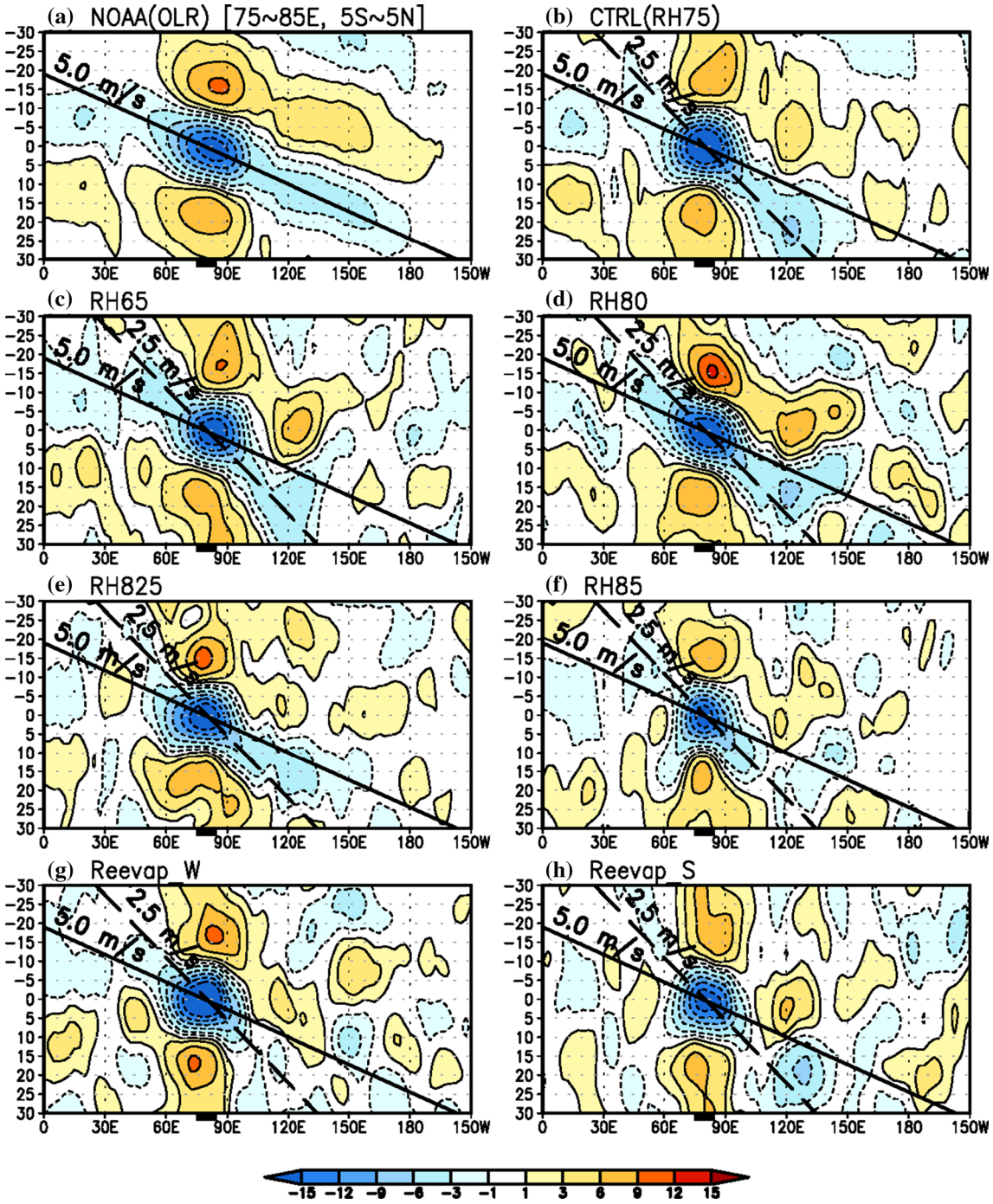

Fig. 6 Lag-longitude cross section of regressed OLR anomalies (contours, intervals of 3.0 W m^{-2} including ± 1.0 W m^{-2}) against the OLR time series at the reference box (5°S–5°N, 75°–85°E) for **a** OBS, and **b–h** NCEP CFS model simulations. Regressed fields are averaged for the latitudes from 10°S to 10°N. The zero contour is omitted and the *black rectangles* in the abscissa denote the locations of the reference points. For each panel, the slanted solid (*long-dashed*) *line* represents phase speed of 5.0 m s^{-1} (2.5 m s^{-1})

rainfall (>10 mm day^{-1}) with enhanced evaporation. A signal-to-noise ratio in wavenumber–frequency spectral domain shows that all CFS experiments tend to simulate spectral signal at slightly lower frequencies (from part of an overreddened spectrum) and higher wavenumbers than the observed (except for RH85). However, RH825 and Reevap_S generate a more realistic spectral band at periods near 50–55 days and wavenumber 1 (except for Reevap_S with wavenumber 3). Furthermore, in these two simulations the eastward-moving signal and the structure of dynamic

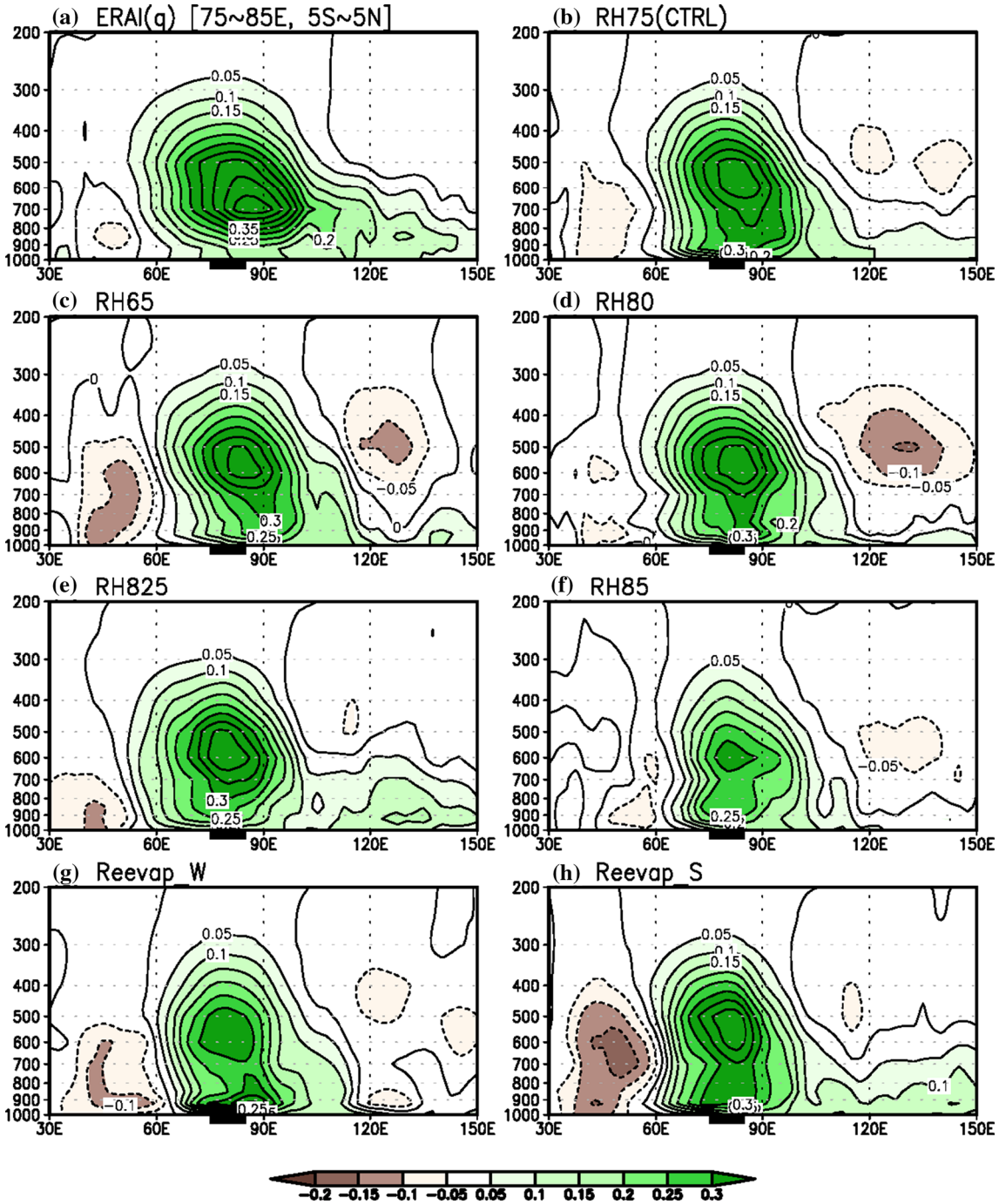

Fig. 7 Longitude–height cross section of regressed specific humidity anomalies (contours, intervals of 0.05 g kg^{-1}) on lag day 0 against the OLR time series at the reference box (5°S–5°N, 75°–85°E) for **a** OBS, and **b–h** NCEP CFS model simulations. Regressed fields are averaged for the latitudes from 10°S to 10°N. The *black rectangles* in the abscissa denote the locations of the reference points

and thermodynamic variables associated with the MJO are better organized than the other simulations. Under these humid environmental conditions resulting from rigorous moisture triggers and a higher fraction of re-evaporation of convective rainfall, the atmosphere is preconditioned by existence of more active shallow cumulus and congestus clouds, leading to more moistening and warming in the lower troposphere. The subsequent enhanced deep convection induces more a humid environment owing to increased detrainment, leading to a higher potential for a more organized convective system, consistent with the

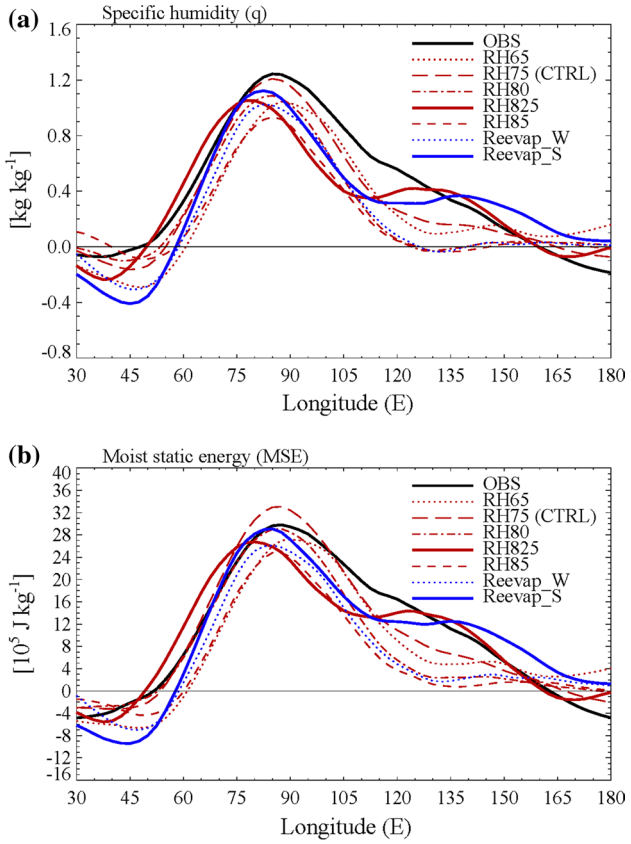

Fig. 8 As in Fig. 7, but for vertically integrated (from the surface to 600 hPa) fields of regressed **a** specific humidity and **b** moist static energy against the OLR time series at the reference box (5°S–5°N, 75°–85°E)

moisture–stratiform instability theory proposed by Mapes (2000) and Kuang (2008).

Recent analyses on the observational data from the 2011 Dynamics of the MJO (DYNAMO) field campaign provided insights into the three-dimensional MJO structure (Hagos et al. 2014, 2016; Wang et al. 2015; Xu and Rutledge 2014). Here we analyzed these DYNAMO CSU Array–Averaged products (Johnson and Ciesielski 2013; Ciesielski et al. 2014) over the Northern Sounding Array (NSA) region. The Wheeler–Hendon real-time multivariate MJO (RMM) index (Wheeler and Hendon 2004) is used to classify MJO phase. The following results, which are consistent with the previous findings, are confirmed: (1) coherent moisture–convection relationship (Fig. 10a; similar to those from ERAI as shown in Fig. 3a), (2) shallow-to-deep-to-stratiform moistening (or moist static energy) transition during MJO life cycle (Fig. 10b, c; similar to Figs. 7a, 8), and (3) bottom-heavy heating profile at the preconditioning stage, top-heavy heating profile at the mature and trailing phases, and cooling profile during suppressed phase (Fig. 10d; similar to Fig. 9).

On the other hand, cloud–radiative interaction is considered to be an essential processes to simulate the realistic MJO (Del Genio and Chen 2015; Jiang et al. 2011; Kim et al. 2015; Ma and Kuang 2011). To investigate the role of cloud–radiative interaction, we plotted the column integrated net radiative heating vs precipitation anomalies regressed onto the OLR time series measured at the reference box of the equatorial central Indian Ocean (5°S–5°N, 75°–85°E), as done in Del Genio and Chen (2015). Only

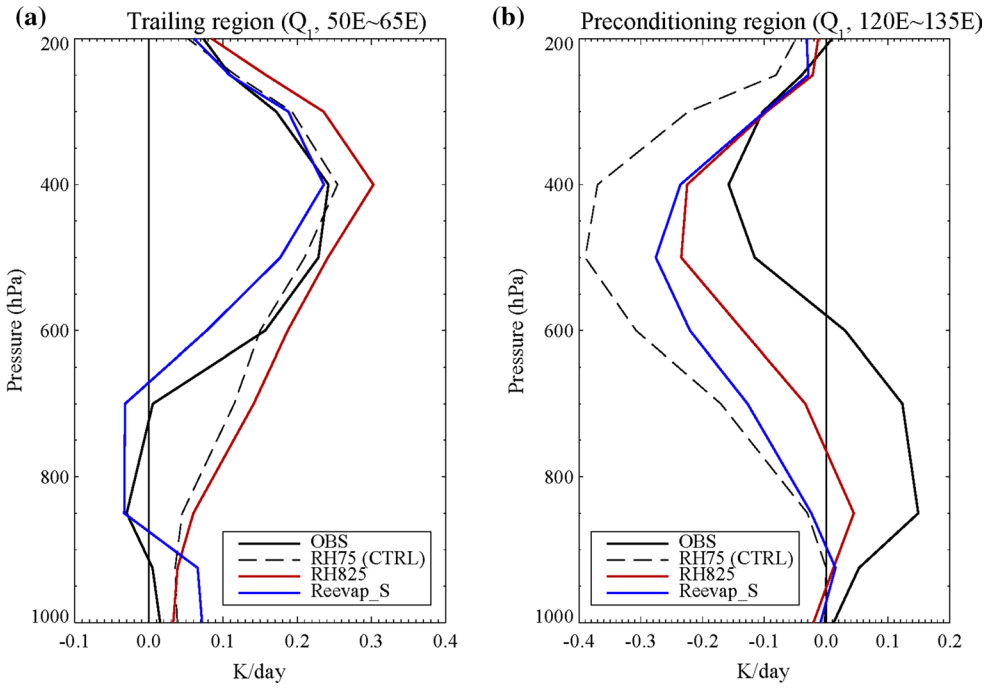

Fig. 9 As in Fig. 7, but for vertical profiles of regressed apparent convective heat source (Q_1, in unit of K day^{-1}) for RH75 (CTRL), RH825, and Reevap_S, averaged over **a** trailing (10°S–10°N, 50°–65°E) and **b** preconditioning (10°S–10°N, 120°–135°E) region

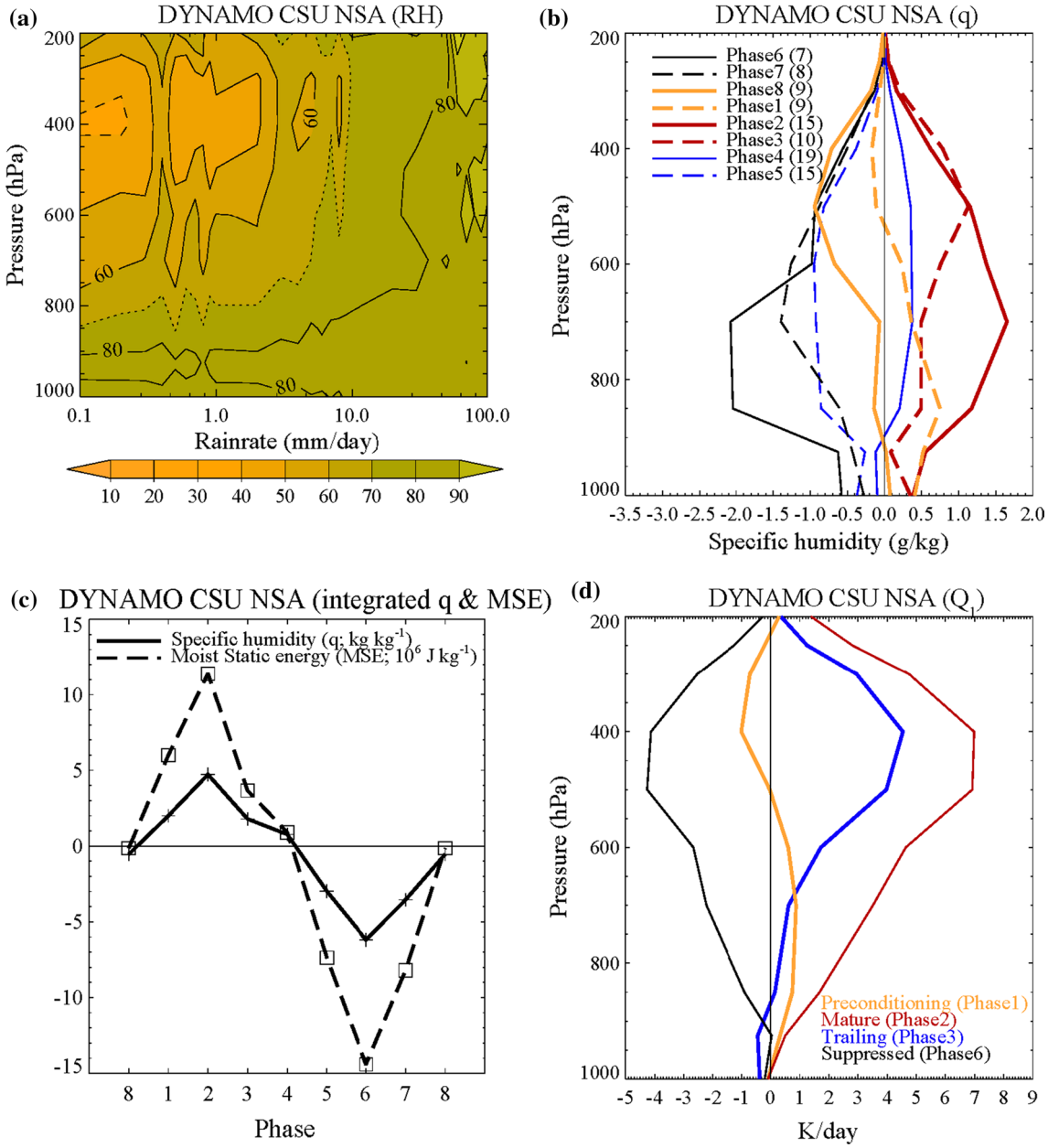

Fig. 10 Composite fields of the DYNAMO CSU 3-month sounding products averaged over the NSA region: **a** vertical structure of relative humidity relative to precipitation rate in TRMM 3B42v7, **b** vertical profile of specific humidity anomalies, **c** vertically integrated (from the surface to 600 hPa) specific humidity and moist static energy, and **d** vertical profile of apparent convective heat source (Q_1) as a function of the WH RMM index. In **b**, the figures in parenthesis indicate the number of each MJO phase during 01 Oct 2011–31 Dec 2011. In **d**, because the NSA region represents phases 2 or 3 in WH RMM index, phase 1, 2, 3, and 6 corresponds to preconditioning, mature, trailing, and suppressed state, respectively

active phase (around zero lag) is plotted in Fig. 11. From this plot, it is seen that both the column net radiative heating and precipitation anomalies are greater in RH825 (Reevap_S) than in RH65 (Reevap_W, respectively), implying that cloud–radiative interaction acts to enhance the intraseasonal activity. Similarly, for the nearly same net radiative heating anomalies (say, lag −5 days for RH825 and RH65 in Fig. 11a, or lag −10 days for Reevap_S and Reevap_W in Fig. 11b), RH825 (Reevap_S) produces more precipitation than RH65 (Reevap_W, respectively), suggesting greater efficiency in generating intraseasonal variability in RH825 or Reevap_S. Therefore, the proper cloud–radiative interaction is important in producing the MJO-like variability.

As a complimentary evaluation of the overall performance of the precipitation process in the model, the

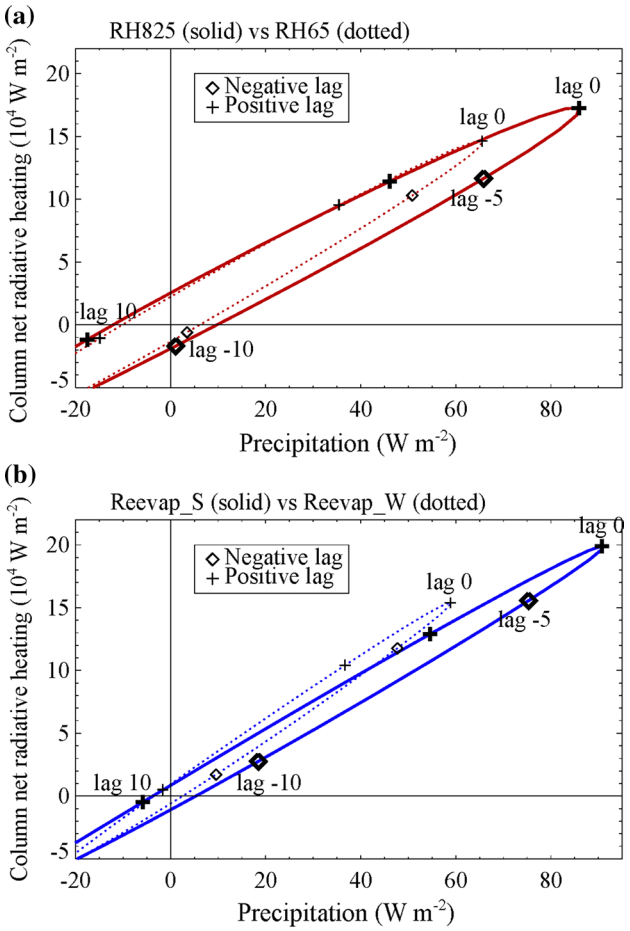

Fig. 11 Time evolution of rainfall anomalies and column integrated (from the surface to 200 hPa) net radiative heating for **a** RH825 and RH65 and **b** Reevap_S and Reevap_W. Both are regressed against the OLR time series at the reference box (5°S–5°N, 75°–85°E) and then averaged over the equatorial central Indian Ocean (10°S–10°N, 75°–85°E). The *crosses* (*diamonds*) represent positive (negative) lag days relative to the OLR time series with every 5 days marked

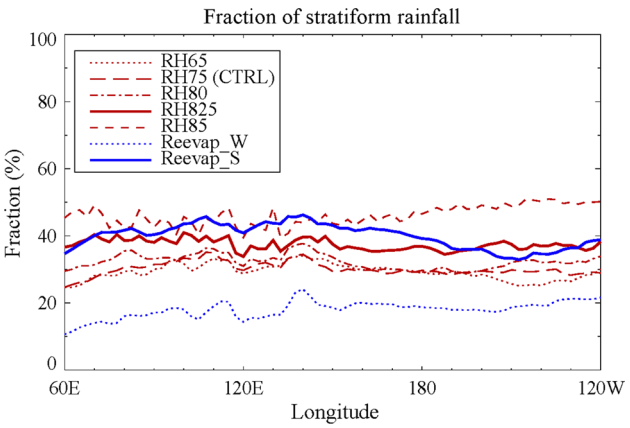

Fig. 12 The fraction of stratiform precipitation to total precipitation over the equatorial warm-pool region (10°S–10°N, 50°–180°E) for each simulation

fraction of stratiform precipitation out of total precipitation over the equatorial warm pool region is depicted in Fig. 12. Especially the stratiform precipitation process plays a critical role in the maintenance of the MJO by elevating a vertical heating profile and generating eddy available potential energy (Fu and Wang 2009; Seo and Wang 2010). In this study, the stratiform rain fraction accounts for ~40 % in RH825 and ~38 % in Reevap_S, which is in very good agreement with the observed ratio described in Schumacher and Houze (2003).

To summarize, our results suggest that the MJO simulation using the coupled CFS with the RAS scheme is sensitive to a moisture triggering parameter and fraction of re-evaporation of convective precipitation, and that a positive relationship between moisture and convection is a necessary key factor for simulating a realistic MJO. However, there remain some deficiencies in RH825 and Reevap_S. For example, the variance of the MJO disturbance (Fig. 5) and the shallow (bottom-heavy) heating or low-level moisture convergence prior to deep convection (Fig. 9b) are weaker than in the observation, even though these magnitudes are larger than in other simulations. Furthermore, the MJO simulations associated with the relaxation parameter of mass flux for adjustment of the environment and the evaporation rate from large-scale precipitation produce a considerable amount of light rainfall and higher signal-to-noise ratio at lower frequencies and higher wavenumbers than the observation (not shown). Therefore, there still exist many physical processes that are in need of improvement.

Acknowledgments The authors thank the two anonymous reviewers for their constructive and helpful comments that improved the manuscript. This work was supported by the National Research Foundation of Korea (NRF) grants funded by the Korea government (MSIP) (Nos. NRF-2014R1A2A1A11051818 & NRF-2015R1A2A2A01006663). The authors would like to acknowledge the support from the Korea Institute of Science and Technology Information (KISTI).

References

Arakawa A, Schubert WH (1974) Interaction of a cumulus cloud ensemble with the large scale environment. Part I. J Atmos Sci 31:674–701

Bladé I, Hartmann DL (1993) Tropical intraseasonal oscillations in a simple nonlinear model. J Atmos Sci 50:2922–2939

Bretherton CS, Peters ME, Back LE (2004) Relationships between water vapor path and precipitation over the tropical oceans. J Clim 17:1517–1528

Cheng MD, Arakawa A (1997a) Inclusion of rain water budget and convective downdrafts in the Arakawa–Schubert cumulus parameterization. J Atmos Sci 54:1359–1378

Cheng MD, Arakawa A (1997b) Computational procedures for the Arakawa–Schubert cumulus parameterization: Tech. Rep. No. 101, Department of Atmospheric Sciences, University of California, Los Angeles, pp 50

Ciesielski PE et al (2014) Quality-controlled upper-air sounding dataset for DYNAMO/CINDY/AMIE: development and corrections. J Atmos Ocean Technol 31:741–764

Dee DP et al (2011) The ERA–Interim reanalysis: configuration and performance of the data assimilation system. Q J R Meteorol Soc 137:553–597. doi:10.1002/qj.828

Del Genio AD, Chen Y (2015) Cloud-radiative driving of the Madden–Julian oscillation as seen by the A-Train. J Geophys Res Atmos 120:5344–5356. doi:10.1002/2015JD023278

Fu X, Wang B (2009) Critical roles of the stratiform rainfall in sustaining the Madden–Julian oscillation: GCM experiments. J Clim 22:3939–3959

Hagos SM, Feng Z, Landu K, Long CN (2014) Advection, moistening, and shallow-to-deep convection transitions during the initiation and propagation of Madden–Julian Oscillation. J Adv Model Earth Syst 6:938–949

Hagos SM, Feng Z, Burleyson CD, Zhao C, Martini MN, Berg LK (2016) Moist process biases in simulations of the Madden–Julian Oscillation episodes observed during the AMIE/DYNAMO field campaign. J Clim 29:1091–1107

Huffman GJ, Adler RF, Morrissey MM, Bolvin DT, Curtis S, Joyce R, McGavock B, Susskind J (2001) Global precipitation at one–degree daily resolution from multisatellite observations. J Hydrometeorol 2:36–50

Hung M-P, Lin JL, Wang W, Kim D, Shinoda T, Weaver SJ (2013) MJO and convectively coupled equatorial waves simulated by CMIP5 climate models. J Clim 26:6185–6214

Jiang X et al (2011) Vertical diabatic heating structure of the MJO: Intercomparison between recent reanalysis and TRMM estimates. Mon Weather Rev 139:3208–3223

Jiang X et al (2015) Vertical structure and physical processes of the Madden–Julian oscillation: exploring key model physics in climate simulations. J Geophys Res Atmos. doi:10.1002/2014JD022375

Johnson RH, Ciesielski PE (2013) Structure and properties of Madden–Julian oscillations deduced from DYNAMO sounding arrays. J Atmos Sci 70:3157–3179

Kemball-Cook SR, Weare BC (2001) The onset of convection in the Madden–Julian oscillation. J Clim 14:780–793

Kim H-K, Seo K-H (2016) Cluster analysis of tropical cyclone tracks over the western north pacific using a self-organizing map. J Clim 29:3731–3751

Kim D, Sperber K, Stern W, Waliser D, Kang IS, Maloney ED, Wang W, Weickmann K, Benedict J, Khairoutdinov M, Lee MI, Neale R, Suarez M, Thayer-Calder K, Zhang G (2009) Application of MJO simulation diagnostics to climate models. J Clim 22:6413–6436

Kim D, Xavier P, Maloney ED, Wheeler M, Waliser D, Sperber K, Hendon H, Zhang C, Neale R, Hwang Y-T, Liu H (2014) Process-oriented MJO simulation diagnostic: moisture sensitivity of simulated convection. J Clim 27:5379–5395

Kim D, Ahn MS, Kang IS, Del Genio AD (2015) Role of longwave cloud-radiation feedback in the simulation of the Madden–Julian oscillation. J Clim 28:6979–6994

Kuang ZM (2008) A moisture–stratiform instability for convectively coupled waves. J Atmos Sci 65:834–854

Liebmann B, Smith CA (1996) Description of a complete (interpolated) outgoing longwave radiation dataset. Bull Am Meteorol Soc 77:1275–1277

Lin JL et al (2006) Tropical intraseaonal variability in 14 IPCC AR4 climate models. Part I: Convective signals. J Clim 19:2665–2690

Ma D, Kuang Z (2011) Modulation of radiative heating by the Madden–Julian oscillation and convectively coupled Kelvin waves as observed by CloudSat. Geophys Res Lett 38:L21813. doi:10.1029/2011GL049734

Madden RA, Julian PR (1994) Observations of the 40–50-day tropical oscillation–a review. Mon Weather Rev 122:813–837

Maloney ED, Hartmann DL (2000) Modulation of eastern North Pacific hurricanes by the Madden–Julian oscillation. J Clim 13:1451–1460

Mapes BE (2000) Convective inhibition, subgrid-scale triggering energy, and stratiform instability in a toy tropical wave model. J Atmos Sci 57:1515–1535

Moorthi S, Suarez MJ (1992) Relaxed Arakawa–Schubert: a parameterization of moist convection for general circulation models. Mon Weather Rev 120:978–1002

Moorthi S, Suarez MJ (1999) Documentation of version 2 of relaxed Arakawa–Schubert cumulus parameterization with convective downdrafts. NOAA Tech. Rep. NWS/NCEP 99-01, p 44

Pacanowski RC, Griffies SM (1998) MOM 3.0 manual. NOAA/Geophysical Fluid Dynamics Laboratory, Princeton. p 668

Saha S et al (2006) The NCEP climate forecast system. J Clim 19:3483–3517

Schumacher C, Houze RA Jr (2003) Stratiform rain in the tropics as seen by the TRMM precipitation radar. J Clim 16:1739–1756

Seo K-H, Son S-W (2012) The global atmospheric circulation response to tropical diabatic heating associated with the Madden–Julian oscillation during Northern winter. J Atmos Sci 69:79–96

Seo K-H, Wang W (2010) The Madden–Julian oscillation simulated in the NCEP Climate Forecast System model: the importance of stratiform heating. J Clim 23:4770–4793

Seo K-H, Schemm JKE, Wang W, Kumar A (2007) The boreal summer intraseasonal oscillation simulated in the NCEP Climate Forecast System (CFS): The effect of sea surface temperature. Mon Weather Rev 135:1807–1827

Sobel AH, Maloney ED (2012) An idealized semi-empirical framework for modeling the Madden–Julian oscillation. J Atmos Sci 69:1691–1705

Sobel AH, Maloney ED (2013) Moisture modes and the eastward propagation of the MJO. J Atmos Sci 70:187–192

Sobel AH, Nilsson J, Polvani LM (2001) The weak temperature gradient approximation and balanced tropical moisture waves. J Atmos Sci 58:3650–3665

Sud Y, Molod A (1988) The roles of dry convection, cloud–radiation feedback processes, and the influence of recent improvements in the parameterization of convection in the GLA GCM. Mon Weather Rev 116:2366–2387

Takayabu YN, Iguchi T, Kachi M, Shibata A, Kanzawa H (1999) Abrupt termination of the 1997–98 El Nino in response to a Madden–Julian oscillation. Nature 402:279–282

Thayer-Calder K, Randall DA (2009) The role of convective moistening in the Madden–Julian oscillation. J Atmos Sci 66:3297–3312

Wang W, Schlesinger ME (1999) The dependence on convection parameterization of the tropical intraseasonal oscillation simulated by the UIUC 11-layer atmospheric GCM. J Clim 12:1423–1457

Wang S, Sobel AH, Zhang F, Sun YQ, Yue Y, Zhou L (2015) Regional simulation of the October and November MJO events observed during the CINDY/DYNAMO field campaign at gray zone simulation. J Clim 28:2097–2119

Wheeler MC, Hendon HH (2004) An all-season real-time multivariate MJO index: Development of an index for monitoring and prediction. Mon Weather Rev 132:1917–1932

Wheeler MC, Kiladis GN (1999) Convectively coupled equatorial waves: analysis of clouds and temperature in the wavenumber–frequency domain. J Atmos Sci 56:374–399

Wheeler MC, McBride JL (2005) Intraseasonal variability in the atmosphere-ocean climate system. In: Waliser DE (ed) Lau WKM. Praxis, Chichester, pp 125–173

Wu Z (2003) A shallow CISK, deep equilibrium mechanism for the interaction between large-scale convection and large-scale circulations in the tropics. J Atmos Sci 60:377–392

Xavier PK (2012) Intraseasonal convective moistening in CMIP3 Models. J Clim 25:2569–2577

Xu W, Rutledge SA (2014) Convective characteristics of the Madden–Julian oscillation over the central Indian Ocean observed by shipborne radar during DYNAMO. J Atmos Sci 71:2859–2877

Yanai M, Esbensen S, Chu J-H (1973) Determination of bulk properties of tropical cloud clusters from large-scale heat and moisture budgets. J Atmos Sci 30:611–627

Zhang C (2013) Madden–Julian oscillation: bridging weather and climate. Bull Am Meteorol Soc 94:1849–1870